Front. Earth Sci. 2016, 10(4): 761–771
DOI 10.1007/s11707-015-0576-6

RESEARCH ARTICLE

Trace Projection Transformation: a new method for measurement of debris flow surface velocity fields

Yan YAN[1,2], Peng CUI (✉)[1,3], Xiaojun GUO[1,2], Yonggang GE[1]

1 Key Laboratory of Mountain Surface Process and Hazards/Institute of Mountain Hazards and Environment, Chinese Academy of Sciences, Chengdu 610041, China
2 University of Chinese Academy of Sciences, Beijing 100049, China
3 Center for Excellence in Tibetan Plateau Earth Sciences, Chinese Academy of Sciences, Beijing 100101, China

Abstract Spatiotemporal variation of velocity is important for debris flow dynamics. This paper presents a new method, the trace projection transformation, for accurate, non-contact measurement of a debris-flow surface velocity field based on a combination of dense optical flow and perspective projection transformation. The algorithm for interpreting and processing is implemented in C ++ and realized in Visual Studio 2012. The method allows quantitative analysis of flow motion through videos from various angles (camera positioned at the opposite direction of fluid motion). It yields the spatiotemporal distribution of surface velocity field at pixel level and thus provides a quantitative description of the surface processes. The trace projection transformation is superior to conventional measurement methods in that it obtains the full surface velocity field by computing the optical flow of all pixels. The result achieves a 90% accuracy of when comparing with the observed values. As a case study, the method is applied to the quantitative analysis of surface velocity field of a specific debris flow.

Keywords debris flow, surface velocity field, spatiotemporal variation, dense optical flow, perspective projection transformation

1 Introduction

Debris flows are sudden, complex, superficial processes that comprise a mixture of soil, rock particles and water (Takahashi, 1978; Cui, 1992; Iverson, 1997). Surface velocity field (SVF) and the spatiotemporal variation of flow velocity are crucial for both the dynamics and engineering of debris flows (Arattano and Marchi, 2000; Marchi et al., 2002; Sederman et al., 2004; Itakura et al., 2005; Calvo and Savi, 2009).

Debris flow SVFs are primarily studied using flow measurement instruments. The existing techniques include image analysis, electromagnetic wave measurement, and cross-sectional measurement (Ren et al., 2002; Hürlimann et al., 2003; Arattano and Marchi, 2005). Image analysis includes particle image velocimetry (PIV) or large-scale PIV (LSPIV), spatial filtering velocimetry (SFV), and the spatiotemporal derivative space method (STDSM) (Genevois et al., 2001; Adrian, 2005). Developed in the late 1970s, PIV and LSPIV consist of instantaneous, multipoint, non-contact laser measurements of fluid dynamics (Costa et al., 2000; Kantoush et al., 2008; Dramais et al., 2011; Zhang et al., 2013). In this method, the measurement area is divided into a number of interrogation areas (IA), and obtains the mean velocity by comparing the characteristics of the search areas (Valentino et al., 2008). The SVF obtained in the previous studies (Ilstad et al., 2004; Fujisawa and Oguma, 2008; Lee et al., 2009) is sparse and of low precision because of the large IA area (Fox and Belcher, 2011; Fujita and Kunita, 2011; Kantoush et al., 2011). Meanwhile, STDSM and SFV provide only an approximate direction of flow, but cannot provide the accurate measurements of the velocity (Leitgeb et al., 2002; Szkulmowski et al., 2008). The result thus provided gives only a mean velocity field after a certain period of measurement, rather than a full velocity vector field.

Electromagnetic wave measurement based on the Doppler Effect obtains only mean flow velocities at one or a few points, but not the continuous field on the entire flow surface (Felberg et al., 2002; Kouamé et al., 2003; Pedersen et al., 2007).

The often adopted flow velocity in practice is actually the mean velocity determined by timing the flow passing through two cross-sections using ultrasonic sensors or

Received July 29, 2015; accepted December 11, 2015

E-mail: pengcui@imde.ac.cn

ground vibration sensors, which describes the movement en masse, but nothing about SVF (Hürlimann et al., 2003; Arattano and Marchi, 2005).

Technically, debris flow velocity measurement and analysis rely on the efficient measurement of SVF and the accurate image distortion correction. Real-time measurement of surface velocity can be achieved by computer vision methods, such as dense optical flow (DOF) and perspective projection transformation (PPT). The DOF correlates the planar motion in two-dimensional (2D) images with the objectives and scenarios in three-dimensional (3D) space, and creates a pattern of moving optical flow. The resulting optical flow contains information of not only the image, but also of the 3D structure (Bouguet, 2001; Farnebäck, 2003; Shi et al., 2014). Therefore DOF can be used to measure the optical flow of all pixels in a fluid motion image as to trace a large cluster of moving objects on flow surface. PPT is widely used for approximating real 3D objects by 2D image (Sidenbladh et al., 2000; Ying et al., 2006; Wang et al., 2008) and also for image distortion correction of fluid motion videos recorded at various angles.

This study aims to propose a new method, the trace projection transformation (TPT), for accurate non-contact measurement of debris flow SVFs, based on DOF and PPT. The accuracy of the proposed method is tested via comparison with data collected from both field observations and laboratory experiments. Subsequently, it is applied for characterizing debris flow dynamics and applications of TPT in variations of debris flow surface velocity.

2 Methodology

2.1 Accurate SVF measurement using orthographic images

Figure 1 gives the schematic illustration of the coordinate for SVF measurement. The measurement is iteratively conducted for the entire image in grids defined by the positions (x, y). The velocity vectors are then $\left(\frac{\Delta x}{\Delta t}, \frac{\Delta y}{\Delta t}\right)$, with Δt the frame interval. Next, DOF analysis on image pairs yields instantaneous and time-averaged 2D SVFs. According to DOF, the gray scale of each moving pixel within the frame interval remains unchanged (Farnebäck, 2003). Therefore, the gray level of the feature point can be used to trace its position in the next frame (i.e., the next frame interval). The DOF is subsequently obtained by computing the optical flow of all the pixels, i.e., $\left(\frac{\Delta x}{\Delta t}, \frac{\Delta y}{\Delta t}\right)$ (Bouguet, 2001; Shi et al., 2014). Fluid motion video exhibits salient regions with high-contrast colors on the fluid surface, corresponding to the impurities and floating debris. The fluid flow can be observed owing to the presence of these regions in the moving fluid surface. When a continuous fluid is fully segmented, the surface of each segment is approximately planar and thereby allowing for computation of surface velocities. Thus, the velocity distribution can be obtained by computing the velocities in all the segments.

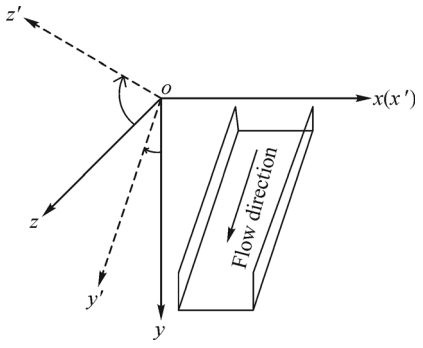

Fig. 1 Schematic of the comparator coordinates, xyz, and the object-space coordinates, $x'y'z'$. Arrows indicate the direction of flow; xoy is the imaging plane of the video; $x'oy'$ is the real plane of the flow.

2.2 Image distortion correction

Image distortion is corrected by the comparison between the two coordinate systems. Suppose the video camera is mounted directly above and perpendicular to the real plane of fluid flow, $x'oy'$, which overlaps with the image plane xoy at a certain height (Fig. 1). It is then possible to transform the image velocity field of the flow surface to the real SVF (Wang et al., 2008). In practice, it is difficult to directly obtain a video orthographic projection of a fluid surface. Thus, certain algorithms are required to perform a perspective transformation and to correct the video (Ying et al., 2006). Here, PPT was adopted for the video image distortion correction.

3 Development of the trace projection transformation method

The algorithm for interpreting and processing is implemented in C++ and realized in Visual Studio 2012. Compute unified device architecture (CUDA) is used to accelerate the calculation. The TPT is used to analyze debris flow videos and support real-time measurement of SVF using a digital video camera. These require a high angle view of the video in continuous proximity to the flow. Shooting angle in the experiment is as high as possible and the distance from the point of lens view is as close as possible. A simpler method for conducting PPT would be to shoot a slightly distorted image at a higher view and orthographic projection. In addition, field surveys before and after the record are necessary to obtain

accurate on-site data, which provide accurate perspective-conversion data for the algorithm and parameter references for establishing video correction and calibration settings.

The procedures for the algorithm implementation are as follows:

1) Image enhancement and restoration: The video is preprocessed to meet the desired conditions. Homomorphic filtering is then used to eliminate the shadow interferences and unstable illumination conditions in the image. Median filtering is then used to eliminate image noises, finishing with shock filtering or smoothing filtering to enhance the image. In this final step, filters are used for image enhancement of the initial video.

2) Image distortion correction and restoration. PPT is adopted for image distortion correction. A 4-point texture mapping is applied on perspective transformation by combining perspective projection and texture mapping.

We set a quadrilateral, $A'B'C'D'$, in xoy in accordance with a reference rectangle, $ABCD$. The algorithm is used to read any static image in the fluid motion video, with $ABCD$ in space corresponding to the quadrilateral $A'B'C'D'$.

A projection rectangle, $A''B''C''D''$, is set in xoy (Fig. 2), which overlaps $A'B'C'D'$ along the sides, i.e., with $A''(x_1'', y_1'')$ overlapping $A'(x_1', y_1')$ and $B''(x_2'', y_2'')$ overlapping $B'(x_2', y_2')$.The length of $A''B''$ is then determined. The length of $B''C''$ and the coordinates of $C''(x_3'', y_3'')$ and $D''(x_4'', y_4'')$ can be determined by using the equation; $\frac{AB}{BC} = \frac{A''B''}{B''C''}$. Then we define p_{ij} as the transformation matrix (PPM) from $x'oy'$ to xoy, with a scaling scalar w (Sidenbladh et al., 2000).

$$\begin{pmatrix} x\cdot w \\ y\cdot w \\ w \end{pmatrix} = \begin{pmatrix} p_{00} & p_{01} & p_{02} \\ p_{10} & p_{11} & p_{12} \\ p_{20} & p_{21} & 1 \end{pmatrix} \begin{pmatrix} x' \\ y' \\ 1 \end{pmatrix}, \tag{1}$$

$$\begin{bmatrix} p_{00} \\ p_{01} \\ p_{02} \\ p_{10} \\ p_{11} \\ p_{12} \\ p_{20} \\ p_{21} \end{bmatrix} = \begin{bmatrix} x_1' & y_1' & 1 & 0 & 0 & 0 & -x_1''x_1' & -x_1''y_1' \\ 0 & 0 & 0 & x_1' & y_1' & 1 & -y_1''x_1' & -y_1''y_1' \\ x_2' & y_2' & 1 & 0 & 0 & 0 & -x_2''x_2' & -x_2''y_2' \\ 0 & 0 & 0 & x_2' & y_2' & 1 & -y_2''x_2' & -y_2''y_2' \\ x_3' & y_3' & 1 & 0 & 0 & 0 & -x_3''x_3' & -x_3''y_3' \\ 0 & 0 & 0 & x_3' & y_3' & 1 & -y_3''x_3' & -y_3''y_3' \\ x_4' & y_4' & 1 & 0 & 0 & 0 & -x_4''x_4' & -x_4''y_4' \\ 0 & 0 & 0 & x_4' & y_4' & 1 & -y_4''x_4' & -y_4''y_4' \end{bmatrix}^{-1} \begin{bmatrix} x_1'' \\ y_1'' \\ x_2'' \\ y_2'' \\ x_3'' \\ y_3'' \\ x_4'' \\ y_4'' \end{bmatrix}. \tag{5}$$

And the scaling scalar is $w = \frac{AB}{A''B''}$.

3) Screenshots from the video are read, with intensities assigned to the grid points.

4) The velocity of characteristic point, V_0, is calculated using DOF. Optical flow is based on the assumption that object points have the same brightness over a short period of time (Δt). Consider point (x, y) in an image $f_t(x,y)$ at time t, then

$$f_t(x,y) = f_{t+\Delta t}(x+\Delta x, y+\Delta y). \tag{6}$$

The optical flow is $\left(\frac{\Delta x}{\Delta t}, \frac{\Delta y}{\Delta t}\right)$. Computing the flow

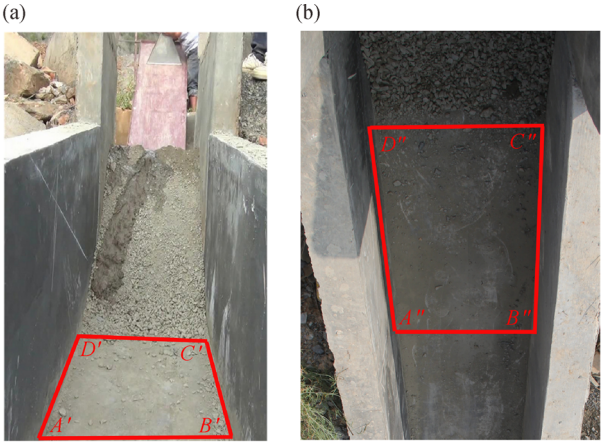

Fig. 2 (a) Positioning of quadrilateral, (b) projection mapping of the projection rectangle's area in the perspective projection transformation algorithm.

$$x\cdot w = p_{00}\cdot x' + p_{01}\cdot y' + p_{02}$$

$$\text{and } w = p_{20}\cdot x' + p_{21}\cdot y' + 1. \tag{2}$$

Eqs. (1) and (2) yield

$$x = p_{00}\cdot x' + p_{01}\cdot y' + p_{02} - p_{20}\cdot x\cdot x' - p_{21}\cdot x\cdot y', \tag{3}$$

$$y = p_{10}\cdot x' + p_{11}\cdot y' + p_{12} - p_{20}\cdot y\cdot x' - p_{21}\cdot y\cdot y'. \tag{4}$$

For the transformation above, only four pairs of observation points were required to solve the coefficient matrix (i.e., PPM).

Similarly, the PPM of the projection rectangle $A''B''C''D''$ and the quadrilateral $A'B'C'D'$ is defined as

vector at every point in the image gives the dense optical flow field (Farnebäck, 2003). The displacement for a point $(x_{current},y_{current})$ can be defined as the displacement $(\Delta x,\Delta y)$ which minimizes the residual error ε between the images:

$$\varepsilon(\Delta x,\Delta y)=\sum_{i=x_{current}-w}^{x_{current}+w}\sum_{j=y_{current}-w}^{y_{current}+w} f_t(x,y)-f_{t+\Delta t}(x+\Delta x,y+\Delta y), \tag{7}$$

where a small $\{(2w+1)$ by $(2w+1)\}$ rectangular region around the current point is used to assess the similarity of images.

This actually implies that

$$\frac{\partial f}{\partial x}\Delta x+\frac{\partial f}{\partial y}\Delta y+\frac{\partial f}{\partial t}\Delta t=0, \tag{8}$$

which can be rewritten as

$$\left(\frac{\partial f}{\partial x}\frac{\partial f}{\partial y}\right)\begin{pmatrix}\frac{\Delta x}{\Delta t}\\ \frac{\Delta y}{\Delta t}\end{pmatrix}=-\frac{\partial f}{\partial t}. \tag{9}$$

Analyzing the fluid motion video: $\frac{\partial f}{\partial x},\frac{\partial f}{\partial y},\frac{\partial f}{\partial t}$ yield's the data matrices, for which the pseudo-inverse matrices $\frac{\Delta x}{\Delta t}$, $\frac{\Delta y}{\Delta t}$ define the pixel-level flow velocity field (i.e., V_0 in xyz).

5) Determination of V' in xoy by V_0 through coordinate transformation. Ground reference points (GRP) were set on both sides of the channel. Real time kinematic (RTK), or total station, was used to measure terrain and obtain the relative coordinates. By using the geometric transformation relation between the object-space coordinates and image coordinates of the control points, image geometric distortion correction was adopted by perspective projection transformation. Additionally, pixel parameters and actual displacement conversion ratios have been used to adjust the size of the image resolution.

6) Determination of surface velocity in $x'oy'$ using PPT. If the height difference between the correction plane and real plane is taken into account, then the object-space coordinates of any point in $x'oy'$ can be obtained by transforming the comparator coordinates of the point in xoy through the PPM. In the comparator coordinates xyz, V' was converted to the actual velocity V in the object-space coordinates $x'y'z'$, namely, the real fluid surface velocity field.

7) Velocity correction. The noise of an image signal often leads to errors and wrong direction in the calculation of velocity. Therefore, it is necessary to correct the velocity field with median filtering after obtaining results. Different from step 1, in which the purpose of filtering was to improve the quality of video images, the filter in step 7 was primarily used to conduct the velocity correction.

Figure 3 shows the procedure used in the TPT method. The hypothesis of perspective projection transformation is a plane. In the plane, surface velocity field is calculated by orthographic projection. In practice, if the gradient of the debris-flow channel bed significantly changes, the channel of debris flow should be divided into separate planes according to different gradients. With corresponding ground reference points set on different planes, and the PPM relationship established within each plane, we can conduct corresponding perspective projection transformation in the different planes.

4 Application

4.1 Application to natural debris flow

These methods were applied to debris flows in Jiangjia Gully, a well-known observation and research site for its active debris flows (Cui et al., 2007; Guo et al., 2013; Li et al., 2015). The flows were then simulated in flume experiments. With the fault intricately distributed, the ravine is deeply cut, steeply sloped, and strongly impacted by frequent tectonic activities. Proterozoic weakly metamorphosed rocks are the most common type found in this ravine, where approximately 80% of the outcrops are highly weathered and are very weak. Phyllite, sandstone and slate are distributed widely in the source areas, resulting in large amounts of loose materials, up to 12.3×10^9 m^3 (Cui et al., 2005). According to the materials distribution and the channel slopes, the main channel is classified into an erosion zone, a transport zone and a deposition zone.

More than 400 debris flows have occurred since 1965, each consisting of numerous surges, at magnitudes varying from thousands to millions of cubic meters, and exhibiting a variety of flow types. Real-time monitoring of debris flow is carried out every rainy season (between May and September) at the Dongchuan Debris Flow Observation and Research Station (DDFORS). The measured parameters include flow depth, velocity, discharge, sediment yield, and so on. Among these, the velocity is traditionally measured as an average value of the surge passing through two fixed cross sections (i.e., the sections A–A' and B–B' in Figs. 4 and 5). For that reason, only the mean velocity of debris flow is measured in observation (Li et al., 2015).

Here we have completed a case study on debris flow events on July 8, 2001 and August 25, 2004, using the proposed TPT method. Both events contain surges of high (1.8–2.2 g/cm^3) and low densities (1.3–1.8 g/cm^3) (Hu et al., 2011b). The traditional mean velocity was obtained by observing the surge fronts passing through two fixed cross-sections in the stream channel (Figs. 4 and 5). Digital

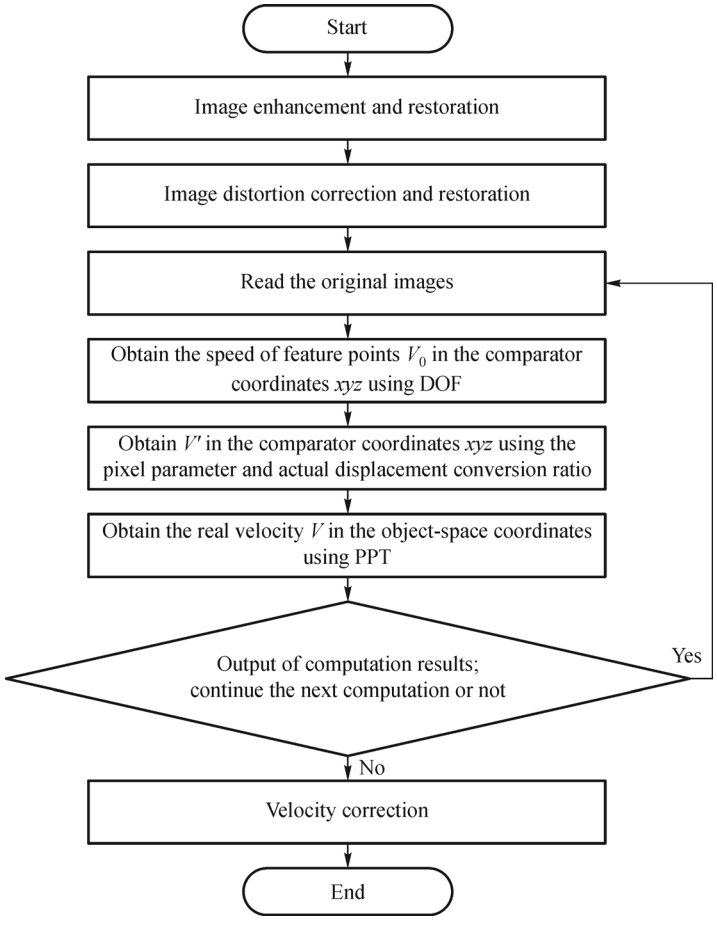

Fig. 3 Flowchart of the trace projection transformation algorithm (loop computation).

Table 1 Comparison of velocities measured by TPT and field observations for the debris flow event on July 8, 2001 (Wei et al., 2002)

Surg number	V_1/(m·s^{-1})	V_2/(m·s^{-1})	Error
1	6.19	6.44	+4.04%
2	6.30	6.01	−4.60%
3	6.74	6.50	−3.56%
4	N/A.	6.22	N/A
5	N/A	6.25	N/A
6	6.02	6.43	+6.81%
7	N/A	6.11	N/A
8	6.87	6.56	−4.51%
9	6.68	6.43	−3.74%
10	5.24	5.51	+5.15%
11	6.36	6.20	−2.52%

video cameras were set facing upstream to record the debris flow motion.

At first we corrected and enhanced the videos taken by DDFORS, which were taken at a side-view and distorted due to the filming equipment on the bank, with shadow interferences due to the unstable light source.

In field observations, homomorphic filtering was adopted to eliminate the shadow interferences and unstable illumination conditions, median filtering was used to eliminate the noises, and in the end, smoothing filtering or shock filtering was employed to enhance the image. Four GRPs in total were set on both sides of the channel. Real Time Kinematic (RTK) or total station was used to measure terrain and obtain the relative coordinates. Image distortion correction and restoration was conducted with the help of the PPT method. As the GRP were set on the bank, there was a height difference between the correction plane and the real plane. In order to eliminate the error, height difference (that was the water level value) was taken into consideration. As a result, the correction plane was similar to the real plane.

4.1.1 Debris flow on July 8, 2001

Videos with an image resolution of 720×576 pixel and a frame rate of 25 fps were used to obtain the mean velocity for each surge. A short shooting distance of 3 m will only a slightly distort an image. The noise of an image signal is weak if the filming spot is located in a deposition zone, and the debris flow is less turbulent. Thus, we corrected the

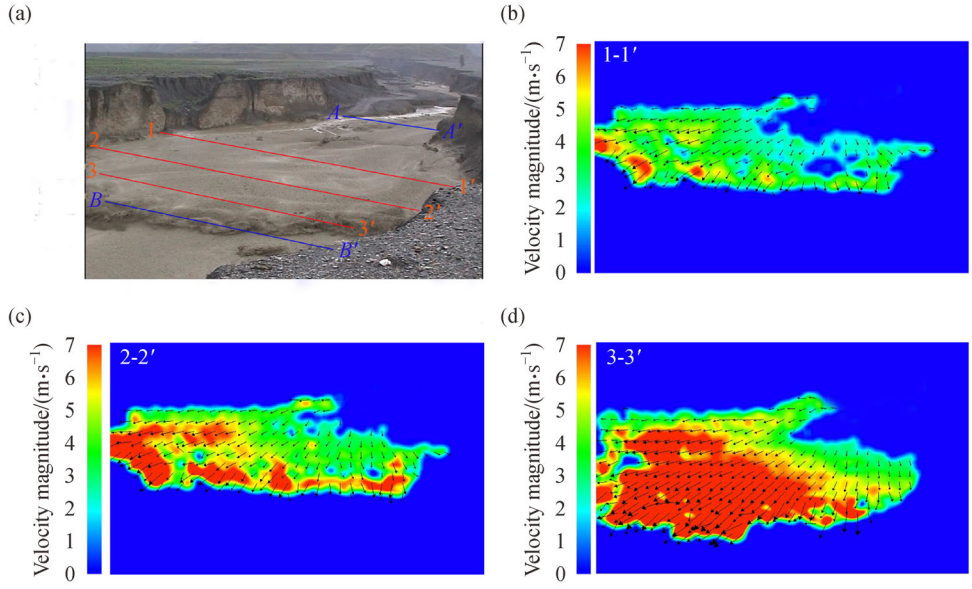

Fig. 4 Schematic diagram of the measurement of surge 1 on July 8, 2001, obtained by using the method described in the text ((a) stands for channel sections; while (b), (c), and (d) represent flow patterns with surface velocity vectors of the surge front at sections 1−1', 2−2', and 3−3', in the observation video, respectively).

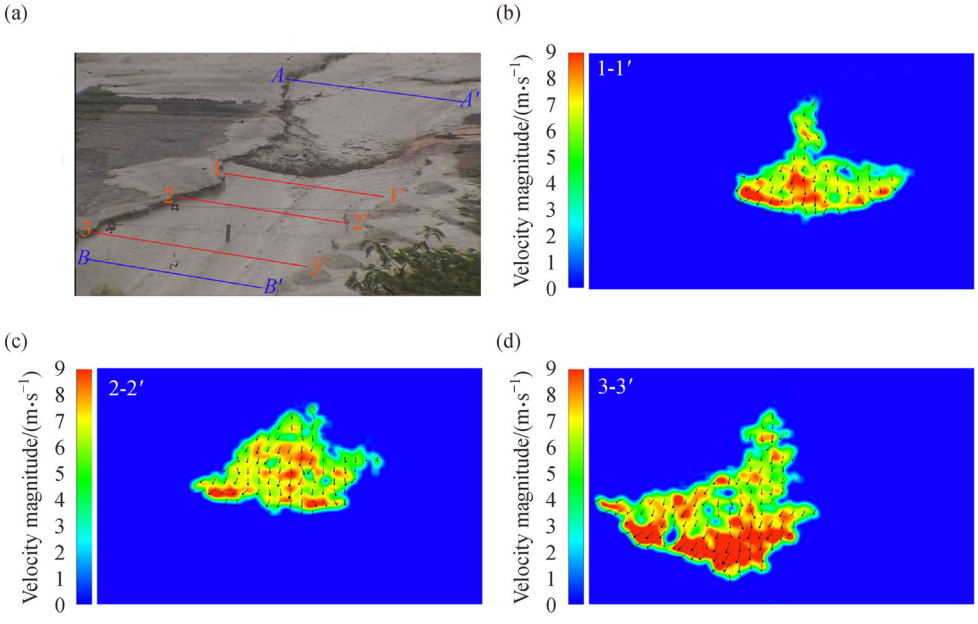

Fig. 5 Schematic diagram of the measurement of the surge 19 front on August 25, 2004, obtained by using the method proposed in this study ((a) represents sections in the channel, while (b), (c), and (d) represent the flow pattern with surface velocity vectors of the surge front at sections 1−1', 2−2', and 3−3', in the observation video, respectively).

velocity through median filtering.

In field measurements, the mean velocity of the surge front is measured based on its travel time between two channel sections, e.g., A–A' and B–B', as shown in Table 1. Figure 4 indicates the velocity field and the flow pattern with surface velocity vectors of the surge front as measured by TPT from image sequences. The mean velocities of the surge front between sections A–A' and B–B' were calculated by:

$$V_2 = \frac{1}{L}\int_0^L V(x)\mathrm{d}x, \tag{10}$$

where, $V(x)$ is the velocity of the surge front at different sections (m/s); and L is the distance between $A-A'$ and $B-B'$ (m). The surge front of the debris flow displayed a typical front-slope shape. As per convention, we defined the length of the surge front as 2 m (Hu et al., 2011a).

The velocities of the surge front were not uniformly distributed. For example, the mean velocity of surge 1 was 6.02 m/s at section 1−1', and increased along the channel, finally reaching 6.67 m/s at section 3−3' (Fig. 4). Based on the velocity field, the mean velocity of surge 1 is 6.44 m/s, following Eq. 10. The TPT test result indicated a deviation of 4.04% when compared with the measured mean velocity of surge 1. The detailed comparison between TPT test results and observation data are listed in Table 1. The result showed that the largest deviation is 6.81%.

4.1.2 Debris flow on August 25, 2004

The event on August 25, 2004 was observed at the end of the transport zone. The channel with a gradient of 123 ‰ and width of 20 m was relatively narrow.

With similar resolution and frame rate, the image of this event differs from the aforementioned one in that: 1) the image was more distorted because of the long shooting distance of 6 m, and 2) the noise was more severe because the turbulent motion and mud splash were more significant. Therefore we combine smoothing and median filtering for velocity correction.

Forty-nine surges were identified from eye-witness reports and videography, 42 of which were measured by a field method (Hu et al., 2011b). The velocities of the surge front between sections $A-A'$ and $B-B'$ were calculated by TPT as V_2 in Table 2. If we take surge 19 as an example, the mean velocity of the surge front is found to be 8.41 m/s at section 1−1', reaching to 8.97 m/s at section 3−3' (Fig. 5), while the mean velocity was 8.73 m/s. A deviation of 3.93% was shown between the TPT test and measured mean velocity of surge 19. The comparison of the overall process between the TPT test results and observation data are listed in Table 2. The results show that the largest deviation is 9.20%.

Table 2 Comparison of velocities measured by TPT and by field observations for the debris flows on August 25, 2004 (Hu et al., 2011b)

Surge number	Timing/(H:M:S)	V_1/(m·s^{-1})	V_2/(m·s^{-1})	Error	Surge number	Timing/(H:M:S)	V_1/(m·s^{-1})	V_2/(m·s^{-1})	Error
1	12:56:00	6.19	6.54	+5.65%	26	13:53:22	6.71	6.90	+2.83%
2	13:07:00	6.19	6.01	−2.91%	27	13:53:58	10.62	11.20	+5.46%
3	13:09:33	6.74	6.50	−3.56%	28	13:56:29	6.95	6.53	−6.04%
4	13:11:09	7.44	6.84	−8.06%	29	13:59:30	6.79	6.47	−4.71%
5	13:12:19	6.25	6.56	+4.96%	30	14:01:41	5.99	6.52	+8.85%
6	13:14:26	6.02	6.43	+6.81%	31	14:03:04	5.88	6.01	+2.21%
7	13:15:05	6.34	5.91	−6.78%	32	14:04:06	6.45	6.40	−0.78%
8	13:16:36	6.87	6.40	−6.84%	33	14:05:41	6.52	6.80	+4.29%
9	13:19:08	6.68	6.54	−2.10%	34	14:06:25	5.61	6.06	+8.02%
10	13:21:57	5.24	5.61	+7.06%	35	14:08:04	6.11	6.43	+5.24%
11	13:22:30	6.36	6.62	+4.09%	36	14:10:25	5.04	4.81	−4.56%
12	13:23:30	6.76	6.20	−8.28%	37	14:10:59	N/A.	5.27	N/A.
13	13:25:12	6.59	6.60	+0.15%	38	14:11:23	5.70	6.00	+5.26%
14	13:27:18	8.40	8.00	−4.76%	39	14:12:09	5.75	6.14	+6.78%
15	13:29:12	6.47	6.01	−7.11%	40	14:13:03	5.88	5.51	−6.29%
16	13:30:12	8.11	8.32	+2.59%	41	14:14:33	N/A.	6.17	N/A.
17	13:33:22	6.39	6.01	−5.95%	42	14:15:22	6.58	6.50	−1.22%
18	13:34:35	5.79	5.50	−5.00%	43	14:16:19	N/A.	6.01	N/A.
19	13:37:24	8.40	8.73	+3.93%	44	14:17:44	4.91	5.20	+5.91%
20	13:39:48	6.82	6.96	+2.05%	45	14:19:01	N/A.	5.67	N/A.
21	13:41:26	6.59	6.43	−2.42%	46	14:20:16	N/A.	6.31	N/A.
22	13:43:38	6.88	6.51	−5.38%	47	14:21:42	5.73	6.16	+7.50%
23	13:45:58	7.00	7.20	+2.86%	48	14:43:12	N/A.	5.13	N/A.
24	13:46:48	11.79	11.54	−2.12%	49	15:00:00	N/A.	5.32	N/A.
25	13:51:07	7.72	7.01	−9.20%					

Note: V_1 and V_2 represent the mean velocity of the surge front observed manually and measured by TPT, respectively.

4.2 Application to flume experiments

We have also applied this method to flume experiments. The flume was 47.3 m long, 0.7 m wide, and 1.2 m high, with a gradient of 20%. The experiments were designed to simulate debris flows from the co-seismic landslide deposition area in Wenjia Gully, located in the Wenchuan earthquake area. The materials taken from the landslide deposit were placed in the flume, and the water was then released upstream to initiate debris flow (Tang et al., 2013). A digital video camera at the flume outlet recorded the entire process. The mean velocity of the surge front was measured by the travel time of the water flow from section *A*−*A*' to section *B*−*B*'. The length of the surge front was identified as 0.2 m.

The image resolution is 1,920×1,080 pixel, the frame rate is 25 fps, and the image distortion is ignorable in comparison with the observation. Given the short shooting distance was measured at 1 m, the correction was conducted with four boundary points of the flume as GRPs. The experiments were initially designed for dam-breaking debris flow formation. Five dams were piled along the flume resulting in extremely turbulent motion and mud splash. In this case, both the median filters and smoothing filters were used in the velocity correction.

If we take Experiment 2 as an example, the mean velocity of the surge front that was calculated by the TPT method gave 4.21 m/s at section 1−1′, which increased along the channel to 4.87 m/s at section 3−3′, resulting in a mean velocity of 4.53 m/s based on the velocity field (Fig. 6). As compared with the practical observation, the error was about 7.86% of the second experiment. The calculated velocities and the compared results are listed in Table 3, indicating the acceptable accuracy of TPT method.

5 Discussion

5.1 Distribution of surface velocity

There are advantages to using the TPT method in the quantitative analysis of the spatiotemporal distribution of surface velocity. As an example, this method was applied

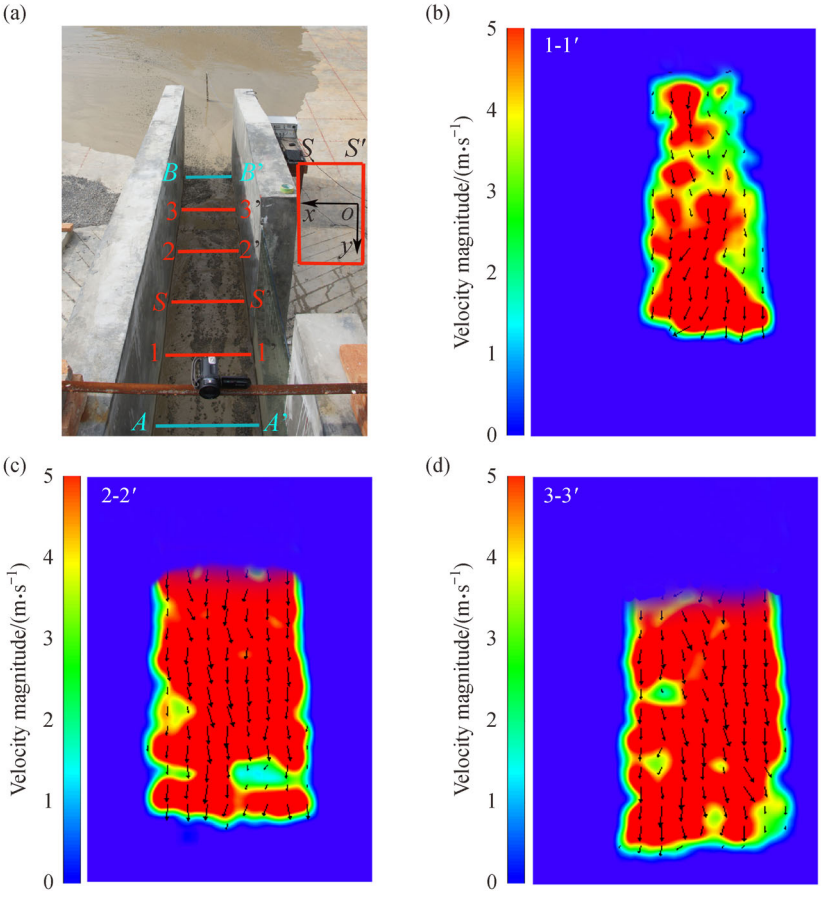

Fig. 6 Schematic diagram of the measurement of the surge front in the second experiment of a series of large-scale flume experiments, measured using the method proposed in this study ((a) denotes channel sections, while (b), (c), and (d) represent flow patterns with surface velocity vectors of the surge front at sections 1−1′, 2−2′ and 3−3′, in the observation video, respectively).

Table 3 Comparison of observed and TPT-measured data in large-scale flume experiments

Experiment number	V_1/ (m·s^{-1})	V_2/ (m·s^{-1})	Error
1	4.11	4.42	+ 7.54%
2	4.20	4.53	+ 7.86%
3	5.60	5.18	− 7.50%
4	2.80	3.03	+ 8.21%
5	4.70	4.54	− 3.40%
6	4.80	5.09	+ 6.04%
7	4.90	5.03	+ 2.65%
8	3.80	3.82	+ 0.53%
9	3.34	3.26	− 2.40%
10	5.50	5.25	− 4.55%
11	5.43	5.01	− 7.73%
12	5.12	4.89	− 4.49%
13	5.56	5.72	+ 2.88%
14	5.00	4.81	− 3.80%
15	4.54	4.75	+ 4.63%

Note: V_1 and V_2 represent the mean velocity of the surge front observed manually and measured by TPT, respectively.

to section S–S' (Fig. 6(a)) in the flume experiment. The section was 0.7 m wide, 0.5 m from the outlet, and perpendicular to the lowest plane of the flume. S–S' represents the section selected for velocity measurement. The coordinate set was established in the S–S' section. The coordinates of the y-axis were not obtained since only the surface velocity was measured.

Figure 7 indicates the distribution of surface velocity at section S–S', varying from point to point (Fig. 7(c)), and corresponding to the velocity field at the 2nd and 6th seconds.

TPT measures the surface velocity field in one section at any time and obtains the mean surface velocity by integral operation of the velocity distribution in that section. The temporal variation of the mean velocity in section S–S' was obtained (Fig. 7(d)). The maximum velocity reached the 2.0 s mark.

5.2 Advancement in the measurement of SVF

Numerous difficulties have been associated with the use of traditional measurement methods of debris flow velocity,

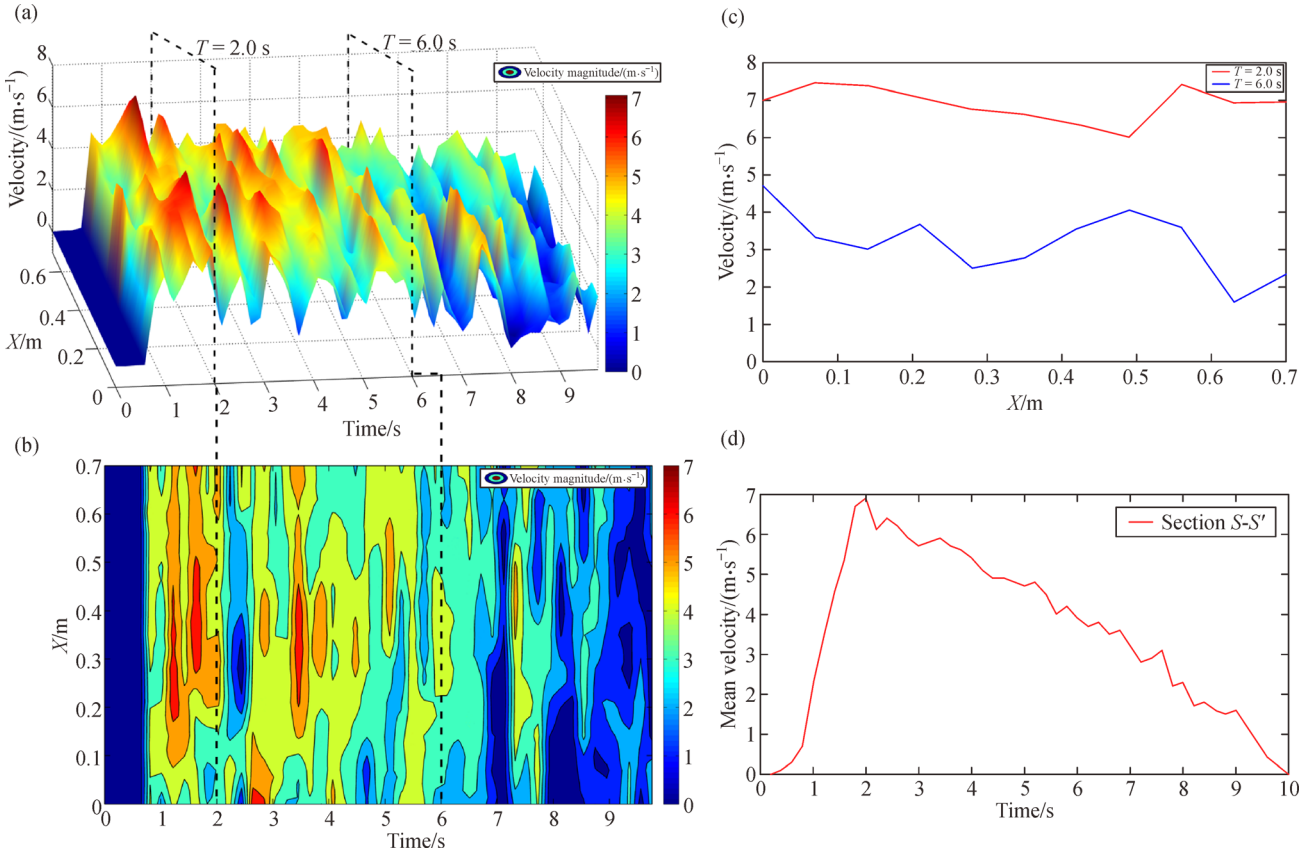

Fig. 7 Spatio-temporal distribution of debris flow surface velocity at section S–S' in Fig. 6(a) ((a) represents spatio-temporal distribution (3D) of debris flow surface velocity; (b) represents a two-dimensional map of the spatio-temporal distribution in debris flow surface velocity; (c) represents the surface velocity at time 2.0 s and 6.0 s; and (d) represents variations in mean surface velocity measured by the proposed method (TPT)).

yet a more accurate measurement method has not yet been determined. 1) The measurement requirements for PIV are steep, typically requiring that tracer particles be manually added. The measurement of debris flow velocity in the field is typically inaccurate, and the velocity field information is often missing. 2) The common method for calculating the mean velocity is to divide the flow distance by time; however, this method cannot measure the temporal and spatial variations. 3) TPT is obviously advanced when compared with traditional measurement methods (Hürlimann et al., 2003; Kouamé et al., 2003; Arattano and Marchi, 2005; Pedersen et al., 2007), because it is able to measure the complete velocity field of the debris flow surface and has been verified in prototype observation and laboratory experiments. It can also achieve the temporal and spatial variations of the surface velocity of debris flow.

TPT strongly depends on the stability of the light source and the camera lens, which is also sensitive to errors generated due to shadow interferences. Therefore, image enhancement and restoration are necessary procedures when using this method.

6 Conclusions

The new TPT method was proposed for an accurate, non-contact measurement of debris flow SVF based on a combination of DOF and PPT. The principle is that the SVF in space can be derived by converting image SVF measured by DOF into the real space of flow through PPT.

TPT was applied using data on natural debris flow processes and large-scale flume experiments. A comparison of this method with the observed values revealed errors of less than 10%, indicating that it can be used to measure the surface velocity of debris flow. TPT will compensate for the inability of the current method to accurately measure the surface velocity fields of the debris flow.

Acknowledgements This study was financially supported by the Key Technologies R&D Program of Sichuan Province (2014SZ0163), the External Cooperation Program of BIC, CAS (131551KYSB20130003), the Open Research Fund by Sichuan Engineering Research Center for Emergency Mapping & Disaster Reduction (K2015B011) and the Key Technologies R&D Program of Sichuan Province (2015SZ0046). The authors thank the DDFORS for providing experimental facilities and data.

References

Adrian R J (2005). Twenty years of particle image velocimetry. Exp Fluids, 39(2): 159–169

Arattano M, Marchi L (2000). Video-derived velocity disribution along a debris flow surge. Phys Chem Earth, Part B Hydrol Oceans Atmos, 25(9): 781–784

Arattano M, Marchi L (2005). Measurements of debris flow velocity through cross-correlation of instrumentation data. Nat Hazards Earth Syst Sci, 5(1): 137–142

Bouguet J Y (2001). Pyramidal implementation of the affine Lucas kanade feature tracker description of the algorithm. Intel Corporation, 5

Calvo B, Savi F (2009). A real-world application of Monte Carlo procedure for debris flow risk assessment. Comput Geosci, 35(5): 967–977

Costa J E, Spicer K R, Cheng R T, Haeni F P, Melcher N B, Thurman E M, Plant W J, Keller W C (2000). Measuring stream discharge by non-contact methods: a proof-of-concept experiment. Geophys Res Lett, 27(4): 553–556

Cui P (1992). Study on conditions and mechanisms of debris flow initiation by means of experiment. Chin Sci Bull, 37: 759–763

Cui P, Chen X Q, Wang Y Y (2005). Jiangjia Ravine debris flows in south-western China. In: Jakob M, Hungr O, editors. Debris-flow hazards and related phenomena(pp. 565–594). Springer Berlin Heidelberg

Cui P, Zhu Y Y, Chen J (2007). Relationships between antecedent rainfall and debris flows in Jiangjia ravine, China. In: Cheng-lung Chen, Jon J. Major, editors. Debris-flow hazards mitigation-mechanics, prediction, and assessment. Rotterdam: Millpress

Dramais G, Le Coz J, Camenen B, Hauet A (2011). Advantages of a mobile LSPIV method for measuring flood discharges and improving stage–discharge curves. J Hydro-environment Res, 5(4): 301–312

Farnebäck G (2003). Two-frame motion estimation based on polynomial expansion. In: Bigun J, Gustavsson T, eds. Image Analysis. Berlin Heidelberg: Springer Verlag, 363–370

Felberg R A, Christou I, Demchuk A M, Malkoff M, Alexandrov A V (2002). Screening for intracranial stenosis with transcranial Doppler: the accuracy of mean flow velocity thresholds. J Neuroimaging, 12 (1): 9–14

Fox J F, Belcher B J (2011). Comparison of macroturbulence measured using decomposition of PIV, ADV and LSPIV data. J Hydraul Res, 49(1): 122–126

Fujisawa N, Oguma Y (2008). Measurement of pressure field around a NACA0018 airfoil from PIV velocity data. J Vis (Tokyo), 11(4): 281–282

Fujita I, Kunita Y (2011). Application of aerial LSPIV to the 2002 flood of the Yodo River using a helicopter mounted high density video camera. J Hydro-environment Res, 5(4): 323–331

Genevois R, Galgaro A, Tecca P R (2001). Image analysis for debris flow properties estimation. Phys Chem Earth, Part C Sol-terr Planet Sci, 26(9): 623–631

Guo X, Cui P, Li Y (2013). Debris flow warning threshold based on antecedent rainfall: a case study in Jiangjia ravine, Yunnan, China. Journal of Mountain Science, 10(2): 305–314

Hu K, Hu C, Li Y, Cui P (2011a). Characteristics and mechanism of debris-flow surges at Jiangjia ravine. In: 5th International Conference on Debris-Flow Hazards Mitigation: Mechanics, Prediction and Assessment.Rome: Casa Editrice Università La Sapienza, 211–217

Hu K, Wei F, Li Y (2011b). Real-time measurement and preliminary analysis of debris-flow impact force at Jiangjia ravine, China. Earth Surf Process Landf, 36(9): 1268–1278

Hürlimann M, Rickenmann D, Graf C (2003). Field and monitoring data of debris-flow events in the Swiss Alps. Can Geotech J, 40(1): 161–

175

Ilstad T, Elverhøi A, Issler D, Marr J G (2004). Subaqueous debris flow behaviour and its dependence on the sand/clay ratio: a laboratory study using particle tracking. Mar Geol, 213(1−4): 415–438

Itakura Y, Inaba H, Sawada T (2005). A debris-flow monitoring devices and methods bibliography. Nat Hazards Earth Syst Sci, 5(6): 971–977

Iverson R M (1997). The physics of debris flows. Rev Geophys, 35(3): 245–296

Kantoush S A, De Cesare G, Boillat J L, Schleiss A J (2008). Flow field investigation in a rectangular shallow reservoir using UVP, LSPIV and numerical modelling. Flow Meas Instrum, 19(3−4): 139–144

Kantoush S A, Schleiss A J, Sumi T, Murasaki M (2011). LSPIV implementation for environmental flow in various laboratory and field cases. J Hydro-environment Res, 5(4): 263–276

Kouamé D, Girault J M, Remenieras J P, Chemla J P, Lethiecq M (2003). High resolution processing techniques for ultrasound doppler velocimetry in the presence of colored noise. Part II: multiplephase pipe-flow velocity measurement. IEEE Trans Ultrason Ferroelectr Freq Control, 50(3): 267–278

Lee S, Park C, Kang J, Daichin (2009). Evaluation of wind environment around a residential complex using a PIV velocity field measurement technique. Environ Fluid Mech, 9(6): 655–668

Leitgeb R, Schmetterer L F, Wojtkowski M, Hitzenberger C K, Sticker M, Fercher A F (2002). Flow velocity measurements by frequency domain short coherence interferometry. Proc SPIE, 4619: 16–21

Li Y, Liu J, Su F, Xie J, Wang B (2015). Relationship between grain composition and debris flow characteristics: a case study of the Jiangjia gully in China. Landslides, 12(1): 19–28

Marchi L, Arattano M, Deganutti A M (2002). Ten years of debris-flow monitoring in the Moscardo torrent (Italian Alps). Geomorphology, 46(1−2): 1–17

Pedersen C J, Huang D, Shure M A, Rollins A M (2007). Measurement of absolute flow velocity vector using dual-angle, delay-encoded Doppler optical coherence tomography. Opt Lett, 32(5): 506–508

Ren H, Brecke K M, Ding Z, Zhao Y, Nelson J S, Chen Z (2002). Imaging and quantifying transverse flow velocity with the Doppler bandwidth in a phase-resolved functional optical coherence tomography. Opt Lett, 27(6): 409–411

Sederman A J, Mantle M D, Buckley C, Gladden L F (2004). MRI technique for measurement of velocity vectors, acceleration, and autocorrelation functions in turbulent flow. J Magn Reson, 166(2): 182–189

Shi B, Wei J, Pang M (2014). A modified optical flow algorithm based on bilateral-filter and multi-resolution analysis for PIV image processing. Flow Meas Instrum, 38: 121–130

Sidenbladh H, Black M J, Fleet D J (2000). Stochastic tracking of 3D human figures using 2D image motion. In: Computer vision—ECCV 2000. Berlin Heidelberg: Springer Verlag, 702–718

Szkulmowski M, Szkulmowska A, Bajraszewski T, Kowalczyk A, Wojtkowski M (2008). Flow velocity estimation using joint spectral and time domain optical coherence tomography. Opt Express, 16(9): 6008–6025

Takahashi T (1978). Mechanical characteristics of debris flow. J Hydraul Div, 104: 1153–1169

Tang J B, Hu K H, Zhou G D, Chen H Y, Zhu X H, Ma C (2013). Debris flow impact pressure signal processing by the wavelet analysis. Journal of Sichuan University: (Engineering Science Edition), 45: 8–13 (in Chinese)

Valentino R, Barla G, Montrasio L (2008). Experimental analysis and micromechanical modelling of dry granular flow and impacts in laboratory flume tests. Rock Mech Rock Eng, 41(1): 153–177

Wang G, Wu Q J, Sun G (2008). Quasi-perspective projection with applications to 3D factorization from uncalibrated image sequences. In: IEEE Conference on Computer Vision and Pattern Recognition, CVPR 2008. IEEE, 1–8

Wei F Q, Hu K H, Cui P, Chen J, He Y P (2002). Characteristics and origing of debris flow of Jiangjiagou valiey blocking. J Soil Water Conserv, 16: 71–75 (in Chinese)

Ying X, Hu Z, Zha H (2006). Fisheye lenses calibration using straight-line spherical perspective projection constraint. In: Narayanan P J, Nayar S K, Shum H Y, eds. Computer Vision–ACCV. Berlin Heidelberg: Springer Verlag, 61–70

Zhang Z, Wang X, Fan T, Xu L (2013). River surface target enhancement and background suppression for unseeded LSPIV. Flow Meas Instrum, 30: 99–111